Journal of Applied Polymer Science

Crystallinity, ion conductivity, and thermal and mechanical properties of poly(ethylene oxide)–illite nanocomposites with exfoliated illite as a filler

Ran Zhen, Qianwen Chi, Xingyuan Wang, Kuo Yang, YinShan Jiang, FangFei Li, Bing Xue
Key Laboratory of Automobile Materials, Ministry of Education and Department of Materials Science and Engineering, Jilin University, Changchun 130025, China
Correspondence to: B. Xue (E-mail: xuebing2011@jlu.edu.cn)

ABSTRACT: Illite particles were exfoliated by the intercalation and subsequent deintercalation of dimethyl sulfoxide (DMSO) in the interlayer of illite, and the exfoliated illite particles were used to prepare a novel poly(ethylene oxide) (PEO)–illite nanocomposite. The resulting exfoliated illite and PEO–illite nanocomposites were characterized by X-ray diffraction (XRD), fourier transform infrared (FTIR) spectroscopy, scanning electron microscopy (SEM), differential scanning calorimetry, ion conductivity testing, thermogravimetry analysis, and mechanical testing. The XRD results showed that the acid treatment of illite to exchange K^+ in the interlayer of illite with H^+ was a necessary condition for the DMSO intercalation. SEM micrographs confirmed the exfoliation of the illite particles in the process of DMSO deintercalation from the interlayer of the illite–DMSO intercalation complex. A good dispersion of exfoliated illite in the PEO matrix was also confirmed. A gradual decrease in the PEO crystallinity in the PEO–illite nanocomposites was observed with increasing exfoliated illite concentration. The ion conductivity of the nanocomposites gradually increased with the filler content and reached 3.21×10^{-5} S/cm at an illite concentration of 20 wt %. The formation of an amorphous region around the exfoliated illite was beneficial for Li^+-ion conduction. The ion conductivity significantly increased when the amorphous regions were connected to each other to form a conducting path for Li^+ ions with a high filler concentration of greater than 10 wt %. Meanwhile, the thermooxidative stability and mechanical properties of the PEO–illite nanocomposites were also enhanced when exfoliated illite was introduced into the polymer matrix. © 2016 Wiley Periodicals, Inc. J. Appl. Polym. Sci. **2016**, *133*, 44226.

KEYWORDS: clay; composites; nanoparticles; nanowires and nanocrystals; polyelectrolytes

Received 6 May 2016; accepted 25 July 2016
DOI: 10.1002/app.44226

INTRODUCTION

Poly(ethylene oxide) (PEO) is one of the most promising solid polymer electrolytes (SPEs) because of its flexible molecular chain structure and its ability to dissolve salts; this ensures a high ionic mobility. Ion conduction in PEO systems has attracted great attention in terms of both fundamental and applied studies.[1–3] Because of the high crystallinity of PEO, cation transport can only be achieved through local segmental motion; this corresponds to a low ion conductivity of 10^{-7} S/cm or lower. For this reason, many different methods have been used to minimize the concentration of the PEO crystalline phase while maintaining its flexibility and mechanical stability, and this extends over a wide temperature range.[4,5] One of the most effective methods has been the addition of inorganic filler materials to PEO.[6–9]

Among numerous materials that have been tested as fillers, layered clays, for instance montmorillonite (MMT), have become a research focus. Ruiz-Hitzky and Aranda[10] showed that the intercalation of PEO molecules into the silicate layers reduced the polymer crystallization, and this led to a higher conductivity compared to that in PEO systems without clay nanoparticles. Kim *et al.*[11] investigated the effects of organic MMT in the PEO matrix on the ion conductivity and found that polymeric electrolyte nanocomposites containing organic MMT showed a higher conductivity than those with Na^+-MMT because of the increased interlayer spacing of organic MMT. Zhang *et al.*[12] also prepared a PEO–MMT SPE with octadecylamine-modified MMT as the filler with the aim of improving the lithium-ion conductivity, and the resulting SPE was used for all-solid-state lithium–sulfur batteries. In addition, Chen *et al.*[13] showed that ion-exchanged Li-MMT clays could also be used as fillers to improve the ion conductivity of the PEO matrix.

Most of these research efforts have focused on MMT because of its cationic exchange capacity and its ability to participate in

intercalation and swelling processes. Also, it has been pointed out that the properties of polymer–clay nanocomposites also depend on the type of clay used.[14] This prompted us to survey the possibility of the formation of novel nanocomposites with different types of clays.

Illite is a clay mineral containing one $[Al_2(OH)_4]^{2+}$ octahedral layer sandwiched between two $(Si_2O_5)^{2-}$ tetrahedral sheets.[15] It is a nonexpanding, clay-sized 2:1 layered mineral with potassium as the interlayer cation, and it is more abundant than MMT, composing 50% of mineral materials on earth.[16] Moreover, illite is a mica clay with larger nanolayers, whereas MMT is a smectite clay with smaller nanolayers.[17] The higher aspect ratio, which is due to the larger nanolayers of illite, contributes to enhanced properties, such as mechanical and thermomechanical properties and thermal stability, when a polymer–illite nanocomposite is formed.[17] Hence, illite as an inorganic filler for hybrid organic–inorganic nanocomposites is very attractive from a commercial aspect. The structural characteristics of illite suggest that illite may also be a useful filler for improving certain properties of the PEO matrix, such as the ion conductivity, mechanical properties and thermal stability. Meanwhile, it has been noticed that the particle size of an inorganic filler significantly affects the properties of the polymer matrix. If layered illite can be exfoliated and dispersed homogeneously in the PEO matrix on the nanometer scale, certain properties of the PEO matrix may be significantly improved. However, most studies involving polymer–clay nanocomposites have been about polymer–MMT nanocomposites, and there have been only a few studies about polymer–illite composites as far as we know. Reports on PEO–illite nanocomposites with layer exfoliated illite as an inorganic filler have been very rare.

In this study, we first prepared an illite–dimethyl sulfoxide intercalation complex (ID) with acidified illite and DMSO. Then, the DMSO molecule in the interlayer of ID was deintercalated to form the exfoliated illite. The exfoliated illite was used as a filler to prepare PEO–illite nanocomposites. A series of tests were used to characterize the as-prepared exfoliated illite and PEO–illite nanocomposites. The effects of the exfoliated illite on the crystallinity, ion conductivity, thermal stability, and mechanical properties were studied to evaluate the possibility of this PEO–illite nanocomposite as an SPE.

EXPERIMENTAL

Chemical

Dimethyl sulfoxide [DMSO; analytical reagent (AR)], anhydrous ethanol (AR), 68 wt % HNO_3, lithium perchlorate ($LiClO_4$; AR), PEO (molecular weight = 5.0×10^5), and acetonitrile (AR) were purchased from Beijing Chemical Reagent Co. PEO and $LiClO_4$ were dried in a vacuum oven for 24 h at 50 and 120 °C, respectively. Illite was collected from Antu County (Jilin Province, China), and it was purified before use.

Purification of Illite

A soil slurry was prepared from raw illite (15 wt %) and deionized water (85 wt %) and left overnight. After uniform agitation for 3 h and placement for 0.5 h, the settled impurities were separated out. Then, the upper soil slurry was suction-filtered, dried at 60 °C, and ground; then, it was passed through a 100-mesh screen. The obtained sample was purified illite (PI).

Intercalation and Exfoliation of Illite

Pretreatment of Illite. The PI was pretreated via thermal activation and acidification. The PI was put into a muffle furnace and heated at 600 °C for 1 h. Then, the sample was cooled down to form thermally activated illite.

In the process of acidification, 5 g of PI was added to 100 mL of a 2 *M* HNO_3 solution. The mixture was stirred in a magnetic stirrer and kept at 95 °C for 3 h, and then, it was suction-filtered, washed to neutral with distilled water, and dried at 60 °C to form acidified illite.

Intercalation of Illite. An amount of 2 g of acidified illite, 50 mL of DMSO, and 5 mL of distilled water were mixed. After the mixture was stirred for 1 h with a magnetic stirrer, it was put into a microwave reactor (MKM-H1A, Qingdao Makewave Co., Ltd.) for 50 min. Afterward, the sample was filtered and fully washed with anhydrous ethanol to remove the excess DMSO. After it was dried at 60 °C, the obtained sample, ID, was obtained. To study the effects of the thermal activation and acidification on DMSO intercalation into the interlayer of illite, the PI and thermally activated illite were also subject to the same process as was the acidified illite to prepare ID.

Exfoliation of Illite. In the exfoliation experiment, the mixture containing acidified illite, DMSO and distilled water after microwave treatment but without filtering was put into an ultrasonicator (PL-J40, Dongguan Kangshijie Ultrasonic Co., Ltd.) for 1 h of ultrasonic treatment at 70 °C. Then the mixture was centrifuged at 4000 rpm to separate the precipitate. The obtained precipitate was washed with anhydrous ethanol to remove the excessive DMSO to form the exfoliated illite sample (IDE).

Preparation of the PEO–Illite Nanocomposites

The preparation of the PEO–illite nanocomposites involved first the dispersion of PEO in acetonitrile. Agitation was performed for 6 h at 60 °C so that PEO was completely dissolved in acetonitrile. Then, $LiClO_4$ in a molar ratio of ethylene oxide to Li of 8:1 and different weight percentages of exfoliated illite were added to the solution of PEO and acetonitrile, and another agitation was started for 48 h at 60 °C. The mixtures were poured into Teflon plates and evaporated at 60 °C in a vacuum oven. The samples were denoted as PL–IDE-*X*, where PL means PEO-$LiClO_4$ system and *X* is the percentage mass ratio of IDE. For example, PL–IDE-15 refers to the PEO–illite nanocomposite made from PEO, $LiClO_4$, and 15 wt % IDE (relative to the weight of PEO and $LiClO_4$). For comparison, PI was also used to prepare the PEO–illite composite under the same conditions, and the product was denoted as PL–PI-15, where the mass ratio of PI was 15 wt %. The PL–IDE-0 sample without illite filler was named PEO–$LiClO_4$ (PL).

Characterization

An X-ray diffraction (XRD) study of the prepared samples was performed with an X'Pert PRO diffractometer with Cu Kα radiation (1.5418 Å) at 50 kV and 250 mA.

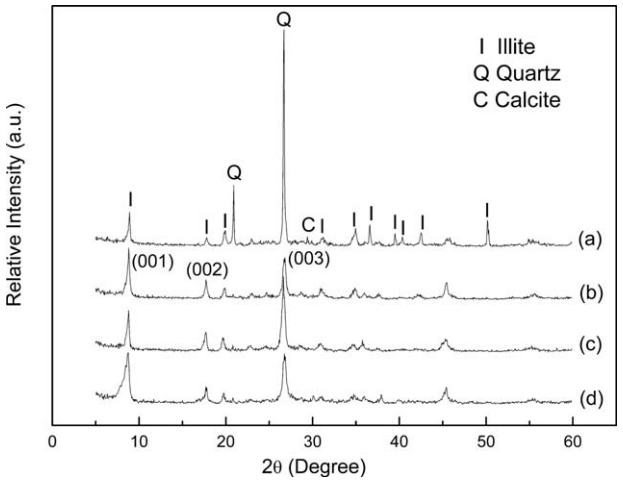

Figure 1. XRD diffraction patterns of the (a) raw illite, (b) PI, (c) thermally activated illite, and (d) acidified illite.

The Fourier transform infrared (FTIR) spectra of the samples were obtained on a Nexus-670 FTIR spectrometer. The samples were prepared as KBr pellets.

A JSM-6700F scanning electron microscope was used to observe the morphologies of the samples at 8 kV.

Differential scanning calorimetry (DSC) analyses was performed with a JY-DSC533 DSC instrument (Shanghai Qingyi Co., Ltd.). The samples were loaded in a sealed aluminum pan, and measurements were done in the range 30–125 °C at a heating rate of 5 °C/min under an N_2 atmosphere.

Impedance spectroscopy was used to determine the ion conductivity of the PEO–illite nanocomposites. The measurements were carried out in the frequency range of 10 Hz-10 KHz (VMP3 potentiostat–galvanostat, Biologic Instruments). The conductivity was measured by the sandwiching of the PEO–illite nanocomposite film between the stainless steel electrodes. The conductivity values (σs) of the nanocomposite systems were calculated from the intercept of real part of the complex-plane impedance plot with the following equation:

$$\sigma = (1/R_b)(t/A)$$

where t is the thickness of the PEO–illite nanocomposite film, R_b is the bulk resistance of the nanocomposite film, and A is the area of the film.[11]

Thermogravimetry analysis (TGA) was performed with a WCT-2C thermoanalyzer (Beijing Optics Apparatus Co., Ltd.). Approximately 10 mg of sample powder was heated in a platinum crucible from 30 to 800 °C at a rate of 10 °C/min under a natural air atmosphere and Al_2O_3 was used as the inert reference. Methods for investigating the thermooxidative stability by TGA included decomposition temperature analysis at weight losses of 10 wt % ($T_{-10\%}$) and 50 wt % ($T_{-50\%}$) obtained from the TGA curves and the mass losses of the polymer between 250 and 400 °C.[18]

The mechanical properties of the prepared PEO–illite nanocomposites were evaluated by tensile testing at room temperature. Samples were cut to dumbbell shapes according to ISO/R 527-1966E. The thickness of each sample was measured at six different points with a micrometer, and the average was taken. Samples were then drawn with a universal testing machine (AG-IS, Shimadzu) at a stretching speed of 20 mm/min. The results presented are the mean values of six independent measurements.

RESULTS AND DISCUSSION

Intercalation and Exfoliation of Illite

XRD Analysis of the Purified and Pretreated Illite. Figure 1 shows the XRD patterns of illite after purification and pretreatment. Obvious characteristic peaks of illite appeared in the XRD pattern of the raw illite, shown in Figure 1(a), and quartz and calcite impurities were also found in the raw illite. After the purification treatment, the diffraction peaks of quartz and calcite almost disappeared from the XRD pattern of PI, shown in Figure 1(b); this indicated that this was an effective purification process for removing impurities. Thermal activation and acidification was performed after the purification process of illite. There was little change in the XRD pattern of the thermally activated illite except for some slight intensity changes in the (001), (002), and (003) lattice planes [Figure 1(c)] when compared to PI; this showed that the heating treatment at 600 °C for 1 h did not obviously influence the structure of illite but only slightly loosened the structure. In comparison, there was a change in the XRD pattern of the acidified illite. As shown in Figure 1(d), the (001) lattice plane of illite became broad and asymmetric; this suggested the elastic deformation of illite layers.[19] This situation resulted from the part cation exchange occurring in the process of the acidification of illite. A certain amount of K^+ in the interlayer of illite was exchanged with H^+ from HNO_3; this led to the deformation of illite layers because of the different sizes of H^+ and K^+ ions.[20] Meanwhile, the octahedral and tetrahedral structures remained stable for the main part of illite after the acid treatment. That was the reason why we observed similar XRD patterns of PI and acidified illite in Figure 2(b,d), except for in the d_{001} reflection shape.

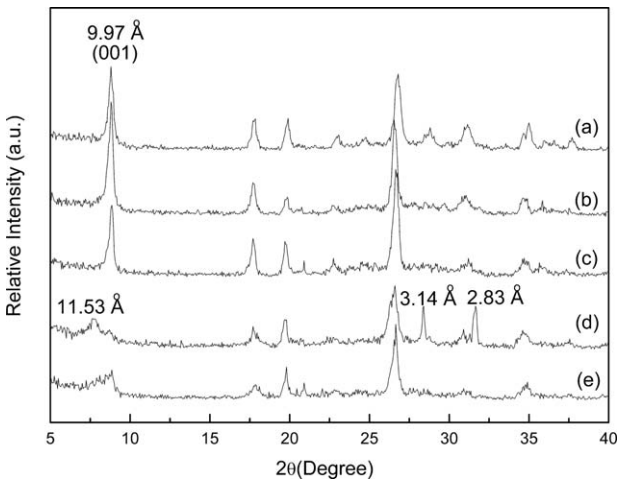

Figure 2. XRD diffraction patterns of the (a) PI and IDs prepared by (b) PI, (c) thermally activated illite, (d) acidified illite, and (e) exfoliated illite.

XRD Analysis of the Intercalation and Exfoliation of Illite. Figure 2 shows the XRD patterns of several IDs. The XRD pattern of PI showed an evident basal d_{001} reflection at a d of 9.97 Å, as shown in Figure 2(a). The d_{001} reflection remained in the same position shown in Figure 2(b) when PI was used to prepare ID; this indicated that no molecules were intercalated into the interlayer of illite. This was mainly due to the nonexpendable nature of mica-type clays.[21,22] Illite is a mica clay with 2:1 layers, and the permanent negative charge of illite is usually balanced by potassium ions, which are located at the planar surfaces of both the clay particles and the interlayers.[23] Those K^+ ions in the interlayers produce tight bonding between layers, and this largely precludes intercalation of DMSO into the layers.[24]

Therefore, pretreatment to activate the lattice of illite and weaken the intense interaction between layers before organic molecule intercalation is very necessary. For the activating clay, thermal activation and acidification have long been used as two major methods.[25–27] In our experiment, thermal activation and acidification were also used to activate the lattice of illite. The thermally activated illite and acidified illite were used to prepare the IDs. As shown in Figure 2(c) the basal d_{001} reflection of illite still remained unchanged, whereas its intensity decreased, and a new d_{001} reflection with a d of 11.53 Å and higher order reflections with ds of 3.14 and 2.83 Å appeared, as shown in Figure 2(d). This showed that DMSO intercalated the interlayer of the acidified illite; this led to a larger interlayer distance. The intercalation ratio (IR) of ID was 66.5%, as calculated from the following equation:

$$\mathrm{IR} = I_1/(I_N + I_1)$$

where I_N and I_1 are the intensities of the (001) diffractions of illite and ID.[28]

These results indicate it was the acidification rather than the thermal activation that fully activated the crystal lattices of illite; this was beneficial for the intercalation of DMSO into the interlayer of illite. Through the analysis of the XRD pattern of acidified illite shown in Figure 1(d), we confirmed that a part of K^+ in the interlayer of illite was exchanged with H^+ from HNO_3; this affected the regular arrangement of illite layers and weakened the strong interaction between the layers. Furthermore, the H^+ exchanged in the interlayer of illite may have played an important role in promoting the intercalation of DMSO.

Figure 2(e) shows the XRD pattern of the exfoliated illite. The disappearance of the d_{001} reflection with a d of 11.53 Å and the enhancement of the intensity of the basal d_{001} reflection are clearly shown in Figure 2(e) compared to Figure 2(d). However, the basal d_{001} reflection of recovery was significantly weakened and broadened; this indicated that the layered structure of illite was less ordered. The cause of the change in the XRD pattern was attributed to the deintercalation of DMSO molecules from the interlayer of ID. The intercalation of the DMSO molecule resulted in a weakening of the layer–layer interactions. When the prepared ID sample without filtering from the mixture was ultrasonicated for 1 h at 70 °C, the DMSO molecules located at the interlayer of ID were removed. The deintercalation of the DMSO molecule from the interlayer of ID disturbed the ordered silicate layer stacking and led to a basal d_{001} diffraction with a reduced intensity and broadened peak.[29] This procedure was similar to the organic molecule intercalation and layer exfoliation of kaolinite and dickite.[30–32]

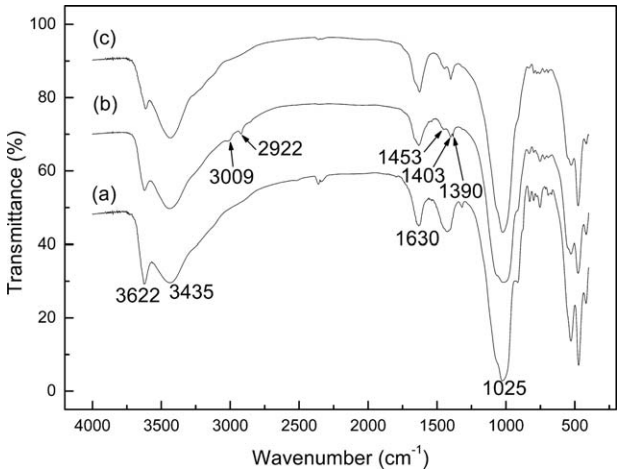

Figure 3. FTIR spectra of the (a) PI, (b) ID, and (c) exfoliated illite.

FTIR Analysis of the Intercalation and Exfoliation of Illite. Figure 3 presents the FTIR spectra of the purified and treated illite. As shown in Figure 3(a), in the 3000–4000-cm^{-1} frequency range, illite exhibited bands at 3622 cm^{-1}, which were attributed to the vibrations of hydroxyls. The broad band at 3435 cm^{-1} was attributed to the OH stretching of hydrogen-bonded water molecules. Absorption bands in the 400–1200-cm^{-1} frequency range were attributed to the vibrations of typical aluminosilicates structural functions. such as Si—O (stretching at 1025 cm^{-1}), Si—O—Si, Si—O—Al, and Al—OH bonds,[15,33] whereas that at 1630 cm^{-1} was attributed to physically adsorbed water molecules on illite platelets. The FTIR spectrum of ID [Figure 3(b)] showed the characteristic absorption bands of DMSO at 1403 and 1453 cm^{-1}, symmetric stretching vibration bands of the methyl group at 3009 and 2922 cm^{-1}, and a symmetrical deformation absorption band of the methyl group around 1390 cm^{-1}. These results prove that the DMSO molecules were inserted into the interlayers of illite. Unlike in the kaolinite–DMSO intercalation complex,[34] the hydrogen bonding of DMSO and hydroxyl groups of the illite did not appear in the FTIR spectrum of ID. This was due to the fact that illite was a phyllosilicate containing one $[Al_2(OH)_4]^{2+}$ octahedral layer sandwiched between two $(Si_2O_5)^{2-}$ tetrahedral sheets.[35] The hydroxyl group of illite, which was between the tetrahedral and octahedral layers, could not come into contact with DMSO. Therefore, the formation of hydrogen bonding between the hydroxyl groups of illite and DMSO was impossible. Illite has a similar 2:1 type structure as MMT, coupled with exchangeable cations in the interlayers, and therefore, organic ammonium cations can intercalate into the interlayers of illite by an ion-exchange reaction.[16,35] However, DMSO molecules are not cations, and the intercalation of DMSO into the interlayer of illite occurred in a different way. We believe that the reaction of DMSO and H^+ in the interlayer

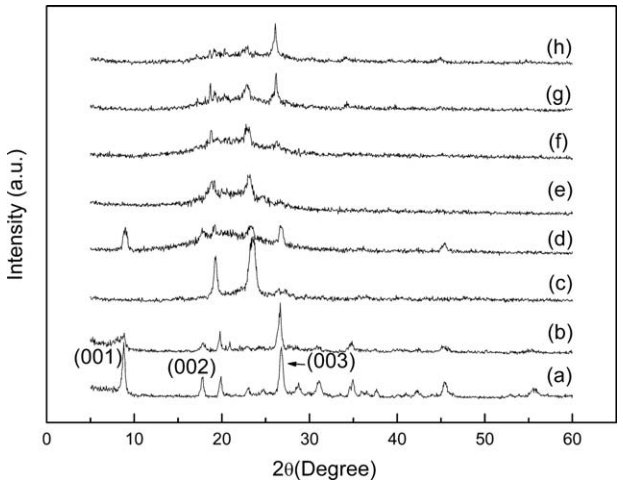

Figure 4. XRD diffraction patterns of the (a) PI, (b) exfoliated illite, (c) PEO–$LiClO_4$, (d) PL–PI-15, (e) PL–IDE-5, (f) PL–IDE-10, (g) PL–IDE-15, and (h) PL–IDE-20.

of illite was the key factor. Before the intercalation reaction, PI was treated by HNO_3 and part of the K^+ in the interlayer of illite was exchanged with H^+ from HNO_3. The S atom center in DMSO is nucleophilic and that makes it easy for DMSO to combine with H^+ and H_2O and form forming $(CH_3)_2SO\cdots H_3O^+$ species by hydrogen bonding.[36] The DMSO molecule may have existed in the form $(CH_3)_2SO\cdots H_3O^+$ in the interlayer of ID. Because the volume of $(CH_3)_2SO\cdots H_3O^+$ was bigger than that of H^+, the intercalation of DMSO caused the expansion of the illite layers and led to the weak interaction between layers. This was the reason that DMSO could only intercalate into the interlayer of acidified illite rather than PI or thermal activated illite. Figure 3(c) shows the FTIR spectrum of the exfoliated illite. The bands of DMSO at 3009 and 2922 cm^{-1} disappeared, as shown in Figure 3(c), but the bands in the 1350–1500-cm^{-1} frequency range were still present in the FTIR spectrum of ID. We confirmed from Figure 2(e) that the DMSO molecule was deintercalated from the interlayer of ID because of the disappearance of the d_{001} reflection with a d of 11.53 Å. Thus, the presence of DMSO bands in the FTIR spectrum of the exfoliated illite were attributed to a small amount of adsorbed DMSO molecules.

Characterization and Performance of the PEO–Illite Nanocomposites

XRD Analysis of the PEO–Illite Nanocomposites. The XRD patterns of the illite samples and various PEO–illite nanocomposites are presented in Figure 4. Compared to PI [Figure 4(a)], the exfoliated illite exhibited a broad basal d_{001} reflection with a low intensity, as shown in Figure 4(b). For PEO–illite nanocomposites containing exfoliated illite filler, the broad basal d_{001} reflection disappeared, as shown in Figure 4(e–h); this indicated the further exfoliation of illite layers during the preparation process and the good dispersion of exfoliated illite in the PEO matrix. In comparison, the basal d_{001} reflection of PI was still prominent when PI was used to prepare the PEO–illite nanocomposite. This indicated that the PL–PI-15 sample was a simple mixture of PEO, $LiClO_4$, and PI [Figure 4(d)]. Meanwhile, the crystallinity change in the PEO–illite nanocomposites with different exfoliated illite contents was also studied by XRD. The characteristic diffraction peaks of the PEO crystalline regions were apparent between 2θs of 19 and 25° [Figure 4(c)]. As shown in Figure 4(e–h), these diffraction peaks became broader and less prominent with the addition of exfoliated illite; this resulted in a decreased crystallinity. With the addition of exfoliated illite to the PEO matrix, the intensities of the characteristic peaks gradually decreased and reached the lowest value for PL–IDE-20.[11] Therefore, the incorporation of exfoliated illite into the PEO matrix increased the amorphous content in the nanocomposites and favored the conductivity of the PEO–illite nanocomposites as SPEs.[12]

FTIR Analysis of the PEO–Illite Nanocomposites

Figure 5 shows the FTIR spectra of the illite samples and various PEO–illite nanocomposites. Figure 5(c) shows the large broad band of asymmetric —CH_2 stretching, which belonged to PEO between 3000 and 2750 cm^{-1}, with two narrow bands at 2741 and 2694 cm^{-1}.[37] The bands around 1145, 1117, and 1088 cm^{-1} were related to the symmetric and asymmetric stretching modes of the C—O—C groups.[38,39] As shown in Figure 5(e), the intensity of these bands in the FTIR region 1200–1000 cm^{-1} decreased when exfoliated illite was added to the PEO matrix. The situation suggests the possible formation of coordination interactions between the ether oxygens of PEO and H^+ from exfoliated illite. The coordination of ether oxygens of PEO with H^+ could have changed the ether oxygen vibrational modes, such as the C—O—C asymmetric and symmetric stretching modes.[38] The results observed from the FTIR spectra are quite similar to those in a literature report on the sodium cations of clay.[37,39] Meanwhile, we observed that the intensity of the C—O—C deformation mode of PL–PI-15, shown in Figure 5(d), was weaker than that of PEO–$LiClO_4$ without any clay filler but was more intense than that of PL–IDE-15. The introduction of PI also influenced the ether oxygen vibrational modes because of the similar coordination interactions between the ether oxygens of PEO and K^+ from PI, but the coordination interactions were weaker than those of PL–

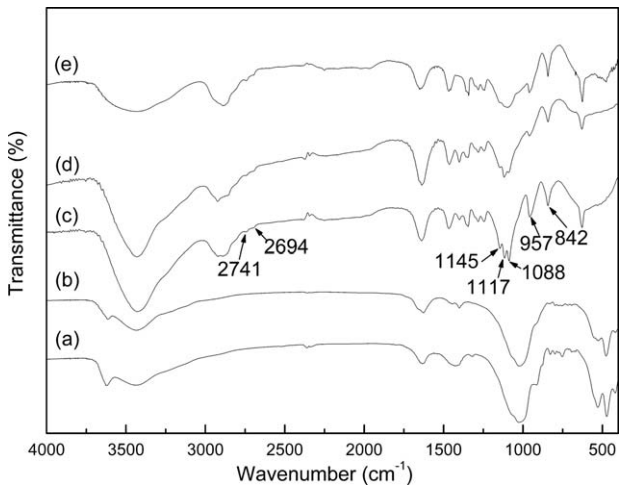

Figure 5. FTIR spectra of the (a) PI, (b) exfoliated illite, (c) PEO–$LiClO_4$, (d) PL–PI-15, and (e) PL–IDE-15.

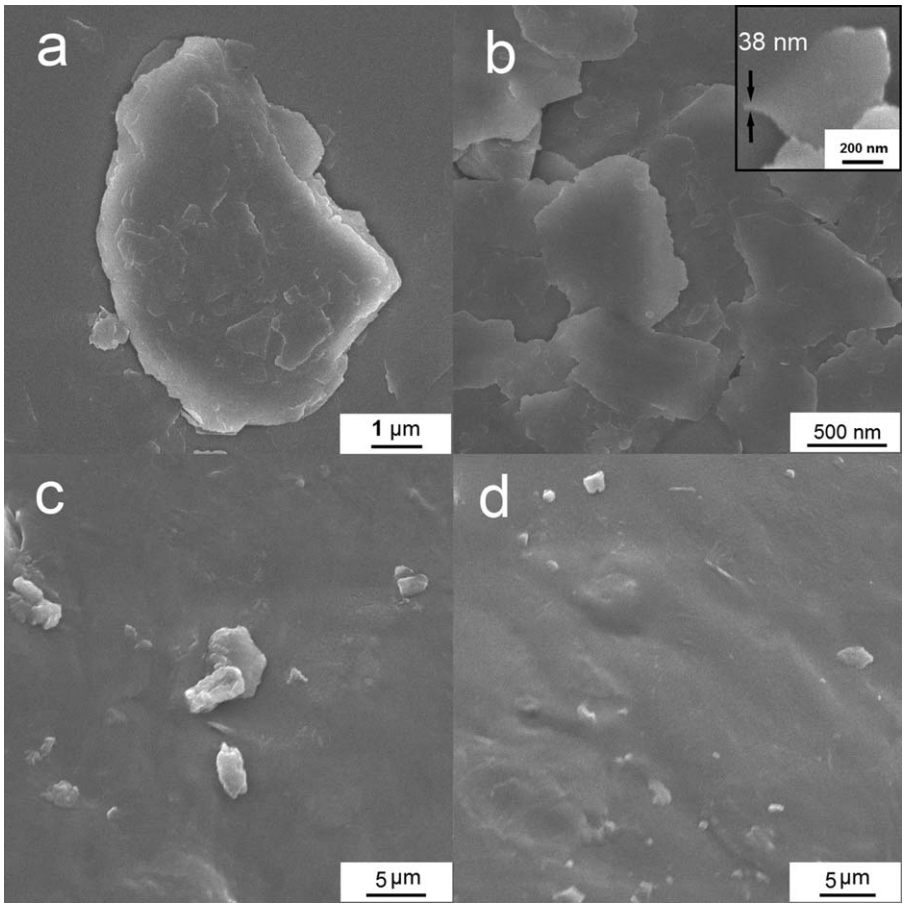

Figure 6. SEM microphotographs of the (a) PI, (b) exfoliated illite, (c) PL–PI-15, and (d) PL–IDE-15.

IDE-15. The H^+ and K^+ located at the surface of the exfoliated illite and PI were involved in the coordination interactions, respectively. For IDE, the illite layers were exfoliated, and more H^+ in the interlayer was exposed to reactions with the ether oxygens of PEO. Therefore, we observed weaker C—O—C asymmetric and symmetric stretching bands in the FTIR spectrum of PL–IDE-15 in Figure 5(e). In addition, according to Ruiz-Hitzky and Aranda's research,[10,40] the bands near 957 and 842 cm^{-1} were assigned to CH rocking vibrations of methylene groups in the gauche conformation required for the helical conformation, so it was generally believed that the PEO was in a helical conformation. The absence of the characteristic PEO band at 1320 cm^{-1} assigned to CH_2 vibrations of the ethylene group in the trans conformation also confirmed the helical structure of PEO.[41] The presence of two bands at 957 and 842 cm^{-1} and the absence of 1320 cm^{-1} in Figure 5(d,e) also suggested that the PEO chains in both PL–PI-15 and PL–IDE-15 had a helical conformation.

Scanning Electron Microscopy (SEM) of the Illite Samples and PEO–Illite Nanocomposites. As indicated by SEM micrographs of PI [Figure 6(a)], the platelike illite particles had a dense layer stacking morphology. The particle size was 0.5–6 μm, and the thickness was 0.2–2 μm. As shown in Figure 6(b), the stacking layers were delaminated, and the particle size of the lamellar illite decreased. The mean diameter of exfoliated illite decreased to about 1 μm, and the thickness reached 25–60 nm. SEM directly displayed the exfoliation of the illite layers and corresponded with XRD and FTIR results. Figure 6(c,d) presents the morphology of the PI and exfoliated illite in the PEO matrix. As shown in the micrograph of PL–PI-15 in Figure 6(c), PI with a larger diameter was not uniformly distributed throughout the PEO matrix. In contrast, PL–IDE-15 displayed a better dispersed morphology, consisting of exfoliated illite layers of different sizes with a small amount of nonexfoliated illite aggregates in an irregular array.

DSC Analysis of the PEO–Illite Nanocomposites. The PEO–illite nanocomposites samples with various concentrations of exfoliated illite were subjected to DSC analysis, as shown in Figure 7. The presence of an intense melting temperature (T_m) indicated the semicrystalline nature of PEO.[37] The intensity of the PEO T_m decreased when exfoliated illite was used as a filler in the PEO matrix because the addition of the exfoliated illite strongly hindered crystallization and decreased the amount of crystalline phase in PEO. The result was consistent with the XRD analysis. This result also shows that illite played the same role as MMT in hindering crystallization of PEO.[37,42] The percentage of crystallinity (X_c) in the nanocomposites was calculated from the ratio of the enthalpy of melting ($\triangle H_m$) per gram of PEO present in the sample to the $\triangle H_m$ per gram of 100% crystalline PEO. Here, $\triangle H_m$ per gram of 100% crystalline PEO

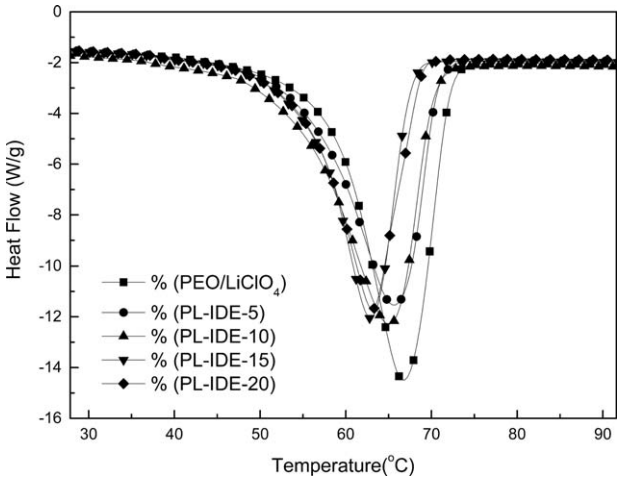

Figure 7. DSC thermograms of the PEO–$LiClO_4$ and PEO–illite nanocomposites with different filler contents.

was taken to be 196.4 J/g.[43] The T_m, $\triangle H_m$, and X_c values of the PEO–$LiClO_4$ and PEO–illite nanocomposites are shown in Figure 8 and Table I. The X_c and $\triangle H_m$ values generally decreased as the amount of exfoliated illite increased. The reduction in X_c was beneficial to the improvement of the ion conductivity of the PEO–illite nanocomposites when these nanocomposites were used as SPEs.[44] The decrease in X_c with the addition of exfoliated illite could be explained by two possibilities: the slowing down of the kinetics of crystallization and the blockage of crystalline growth. These results were caused by the exfoliated illite layers, which were dispersed in an irregular array in the nanocomposite, as was evident from SEM observation as well.[37] In addition, we found that T_m also deceased generally when the amount of exfoliated illite was increased; this corresponded with the $\triangle H_m$ and X_c values.

Ion Conductivities of the PEO–Illite Nanocomposites. The ion conductivities of the PEO–illite nanocomposites with different exfoliated illite contents are presented in Figure 9. The figure indicates that the ion conductivities of the PEO–illite nanocomposites increased as the amount of exfoliated illite increased. The maximum ion conductivity was achieved at a 20 wt % filler

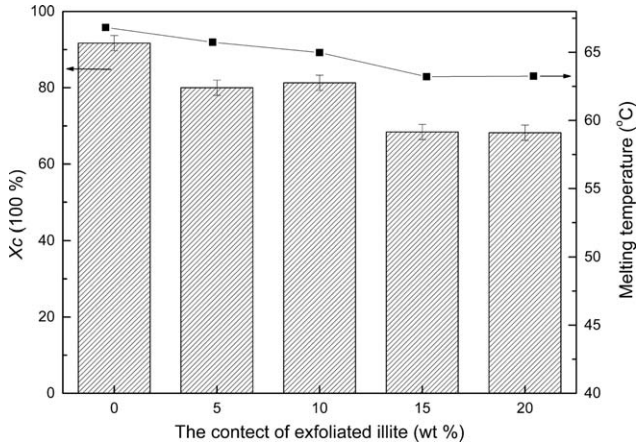

Figure 8. X_c and T_m values of the PEO–$LiClO_4$ and PEO–illite nanocomposites.

Table I. T_m, $\triangle H_m$, and X_c Values of the PEO–$LiClO_4$ and PEO–Illite Nanocomposites

Sample	T_m (°C)	$\triangle H_m$ (J/g)	X_c
PEO–$LiClO_4$	66.83	180.1	91.7
PL-IDE-5	65.74	157.2	80.0
PL-IDE-10	64.98	159.7	81.3
PL-IDE-15	63.21	134.3	68.4
PL-IDE-20	63.25	134.0	68.2

concentration. Also, a rapid increase in the ion conductivity was observed when the content of exfoliated illite exceeded 5 wt %. However, this trend saturated and changed to slightly increase when the content of exfoliated illite exceeded 15 wt %. This increase in the ion conductivity as a function of exfoliated illite addition could have been due to the variation in X_c.[11] The DSC analysis confirmed that the amount of crystalline phase in PEO decreased when exfoliated illite was introduced into the PEO matrix. The exfoliated silicate layers hindered the ordered arrangement of the PEO molecular chain and intercepted the extension of the crystalline phase in the process of nanocomposite preparation. Meanwhile, an amorphous phase with a certain thickness appeared around the exfoliated silicate layers and formed a capsulelike structure. As shown in Figure 10, the core of the capsule was the exfoliated illite layer, and the outer layer of the capsule was the amorphous region, where the Li^+-ion conduction was much faster than the crystalline region for the PEO–$LiClO_4$ system. When the concentration of filler in the PEO matrix was very low, the formed capsules were separated from each other; this meant that the amorphous regions were not connected to each other. For a Li^+ ion moving from one side of the PEO–illite nanocomposite film to another side, the conduction velocity of Li^+ sped up when the ion passed through the amorphous region of the capsules, whereas the velocity was reduced or even stopped when it passed through the crystalline region outside the capsules. The addition of a

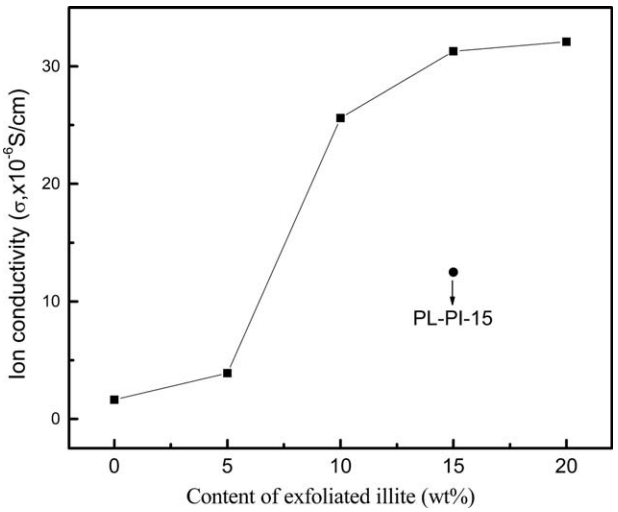

Figure 9. Ion conductivity of the PEO–$LiClO_4$ and PEO–illite nanocomposites

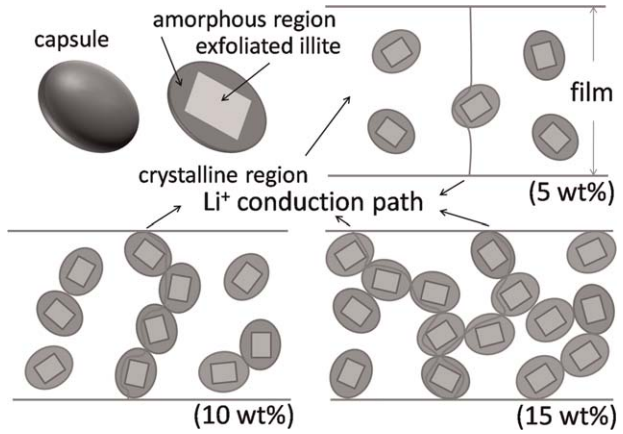

Figure 10. Sketch of the effect of exfoliated illite on the ion conductivity of the PEO–illite nanocomposites

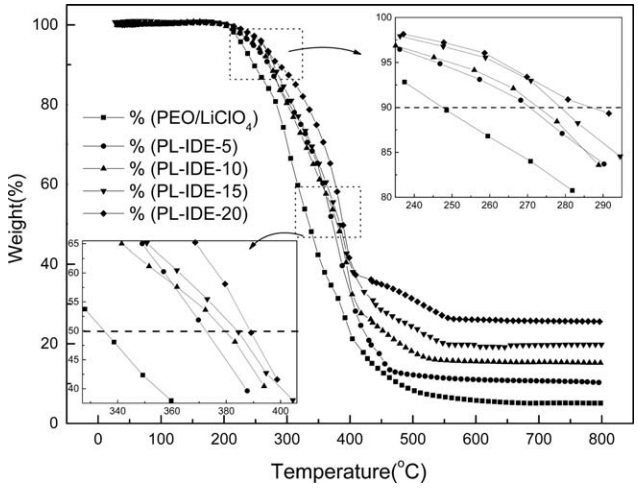

Figure 11. TGA curves of the PEO–$LiClO_4$ and PEO–illite nanocomposites

small amount of exfoliated illite increased the Li^+-ion conductivity of PEO because of the appearance of some amorphous regions around the exfoliated illite, but the improvement in the ion conductivity was not obvious. The situation can is shown in Figure 9 at the point corresponding to 5 wt %. When the filler concentration reached a certain value (10 wt %), the separated capsules were connected to each other to form a network for the transport of Li^+ in the interconnected amorphous regions (see Figure 10); this led to a sharp increase in the ion conductivity. When we continued to increase the filler concentration, more capsules were connected to the network, and more pathways were formed by the connected amorphous region; this resulted in a further improvement in the Li^+-ion conductivity for the PEO–$LiClO_4$ system. However, the increase in the Li^+-ion conductivity was saturated at 15–20 wt %. In addition, PL–IDE-15 exhibited a higher ion conductivity than PL–PI-15. This was attributed to the more completed exfoliation of illite layers and the better dispersion of exfoliated illite in the PEO matrix. At the same filler concentration, exfoliated illite had more silicate layers than PI, and the well-dispersed silicate layers in the PEO matrix were beneficial to the formation of more pathways for Li^+-ion conductivity.

Thermooxidative Stability of the PEO–Illite Nanocomposites. The TGA curves of the PEO–$LiClO_4$ and several PEO–illite nanocomposites are shown in Figure 11. The data of their $T_{-10\%}$ and $T_{-50\%}$ values obtained from the TGA curves and the mass loss of the material between 250 and 400 °C are tabulated in Table II. The thermogravimetric analysis of the PEO–illite nanocomposites (Figure 11) indicated the better thermal stability of the PEO–illite nanocomposites with different amounts of added exfoliated illite compared to the corresponding polymer system without clay. The decomposition temperatures ($T_{-10\%}$ and $T_{-50\%}$) continuously increased as the amount of exfoliated illite was increased. There was an almost 25–55 °C increase (Table II) in the decomposition temperature of those nanocomposites compared with PEO–$LiClO_4$ without clay. Moreover, those PEO–illite nanocomposites exhibited a lower mass loss (250–400 °C) value than PEO–$LiClO_4$, and the mass loss gradually decreased with the addition of exfoliated illite; this indicated an improved thermooxidative stability. The improvement in the thermooxidative stability of the PEO–illite nanocomposites may have depended on two facts. One was the reduced mobility of the polymer chains. Namely, the degradation of PEO started with backbone scission and proceeded by intermolecular and intramolecular transfer reactions, and a typical degradation product was a mixture of monomer and oligomers.[45] The reduced molecular mobility induced by the coordination interactions between the ether oxygens of PEO and H^+ from exfoliated illite suppressed chain-transfer reactions and, consequently, improved the thermal stability of the PEO matrix. The other was the hindered effect of the exfoliated illite platelets on the diffusion of O_2 and volatile products throughout the nanocomposites. This made a further contribution to the improved thermooxidative stability. The combination of these two effects resulted in the PEO–illite nanocomposites exhibiting much

Table II. TGA and Tensile Test Data of the PEO–LiClO4 and PEO–Illite Nanocomposites

Sample	$T_{-10\%}$ (°C)	$T_{-50\%}$ (°C)	Mass loss % (250–400 °C)	Tensile strength (MPa)	Elongation at break (%)
PEO–$LiClO_4$	247.2	334.8	66.6	3.459	183
PL–IDE-5	270.7	372.4	61.5	7.429	253
PL–IDE-10	272.7	379.6	59.7	8.215	287
PL–IDE-15	278.6	383.8	56.7	15.650	421
PL–IDE-20	286.6	388.9	55.6	12.020	423

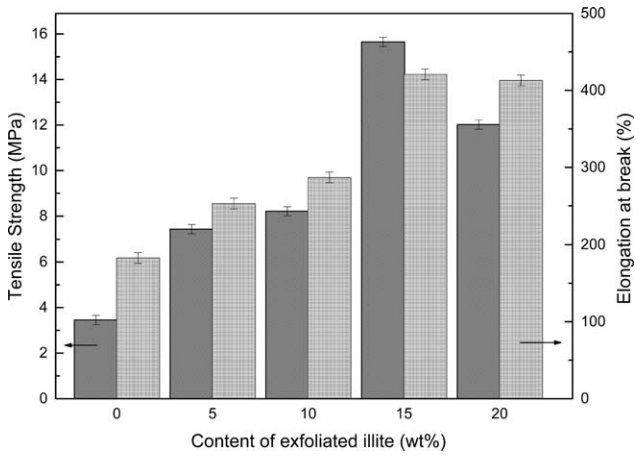

Figure 12. Tensile strength and elongation at break values of the PEO–$LiClO_4$ and PEO–illite nanocomposites.

better thermooxidative properties with respect to the polymer system with the illite filler.

Mechanical Properties of the PEO–Illite Nanocomposites. Tensile testing was conducted to obtain an idea of the effect of different clay loadings on the mechanical behavior of nanocomposites, and the tensile test results are exhibited in Table II and Figure 12. Compared to PEO–$LiClO_4$ without clay, the tensile strength increased with the incorporation of exfoliated illite; it attained a maximum value of 15.65 MPa at 15 wt % clay. This was followed by a significant decrease up to 20 wt %. This result indicated that the incorporation of exfoliated illite up to an optimum level resulted in a considerable reinforcing effect. Moreover, as shown in Figure 12, the elongation at break of the PEO–illite nanocomposites increased and decreased simultaneously with the tensile strength. The improvement in the tensile strength resulted from the ion-exchange reaction in the process of the acid treatment and the exfoliation of illite layers in the PEO matrix; this allowed it to form strong coordination interactions between the ether oxygens of PEO and H^+ from exfoliated illite. The strong coordination interactions increased the tensile strength of the prepared PEO–illite nanocomposites. However, at a high loading of the filler in the polymer matrix, particle aggregation was likely to occur; this led to decreases in the tensile strength and elongation at break.

CONCLUSIONS

ID was prepared with acidified illite and DMSO. The XRD results show that the acid treatment of illite to exchange K^+ in the interlayer of illite with H^+ was a necessary condition for the DMSO intercalation because of the nucleophilic ability of the S atom center in DMSO and the formation of $(CH_3)_2SO\cdots H_3O^+$ species by hydrogen bonding. Effective ultrasonic treatment deintercalated the DMSO molecules from the interlayer of ID and destroyed the regular arrangement of illite layers. SEM micrographs confirmed that the illite layers were exfoliated and better dispersed in the PEO matrix; this was beneficial for decreasing the crystallinity of PEO. Accordingly, the ion conductivity of PEO–illite nanocomposites gradually increased with increasing filler content because of the reduced crystallinity of PEO. The maximum ion conductivity reached 3.21×10^{-5} S/cm at a 20 wt % filler concentration under the experimental conditions. An amorphous phase with a certain thickness appeared around exfoliated illite layers, forming a capsulelike structure. At a high filler concentration (10 wt %), these capsules joined together to form a network structure, and Li^+-ion conductivity took place in the connected amorphous region; this led to a significant increase in the ion conduction. Moreover, the PEO–illite nanocomposites displayed good thermooxidative stability compared to the PEO–$LiClO_4$ system without illite filler. That situation was attributed to the reduced molecular mobility induced by the coordination interactions between the ether oxygens of PEO and H^+ from illite and the hindered effect of exfoliated illite platelets on the diffusion of O_2 and volatile products throughout the nanocomposites. Furthermore, the exfoliated illite also played a reinforcement role in the PEO–illite nanocomposites because of the delamination of illite layers and coordination interactions between the exfoliated illite and the PEO matrix.

Because all of these properties are very important in the performance of SPEs for rechargeable polymer lithium battery applications, illite with exfoliated layers could be a better option for preparing novel PEO-based SPEs.

ACKNOWLEDGMENTS

The authors thank the Natural Scientific Foundation of China (contract grant numbers 41472035 and 51304080) and the Project of Science and Technology Department (Jilin Province, contract grant number 20140204008SF) for financial support.

REFERENCES

1. Bhattacharyya, A. J.; Fleig, J.; Guo, Y. G.; Maier, J. *Adv. Mater.* **2005**, *17*, 2630.
2. Marzantowicz, M.; Dygas, J. R.; Krok, F.; Lasinska, A.; Florjanczyk, Z.; Zygadlo-Monikowska, E.; Affek, A. *Electrochim. Acta* **2005**, *50*, 3969.
3. Marzantowicz, M.; Dygas, J. R.; Krok, F.; Nowinski, J. L.; Tomaszewska, A.; Florjanczyk, Z.; Zygadlo-Monikowska, E. *J. Power Sources* **2006**, *159*, 420.
4. Munshi, M. Z. A.; Owens, B. B. *Solid State Ionics* **1988**, *26*, 41.
5. Huq, R.; Farrington, G. C.; Koksbang, R.; Tonder, P. E. *Solid State Ionics* **1992**, *57*, 277.
6. Loyens, W.; Maurer, F. H. J.; Jannasch, P. *Polymer* **2005**, *46*, 7334.
7. Abraham, T. N.; Siengchin, S.; Ratna, D.; Karger-Kocsis, J. *J. Appl. Polym. Sci.* **2010**, *118*, 1297.
8. Zhang, H.; Maitra, P.; Wunder, S. L. *Solid State Ionics* **2008**, *178*, 1975.
9. Xie, J.; Duan, R. G.; Han, Y.; Kerr, J. B. *Solid State Ionics* **2004**, *175*, 755.
10. Ruiz-Hitzky, E.; Aranda, P. *Adv. Mater.* **1990**, *2*, 545.
11. Kim, S.; Hwang, E. J.; Jung, Y.; Hana, M.; Park, S. *J. Colloid Surface. A* **2008**, *313–314*, 216.

12. Zhang, Y. G.; Zhao, Y.; Gosselink, D.; Chen, P. *Ionics* **2015**, *21*, 381.
13. Chen, W.; Xu, Q.; Yuan, R. Z. *Mater. Sci. Eng. B* **2000**, *77*, 15.
14. Itagaki, T.; Matsumura, A.; Kato, M.; Usuki, A.; Kuroda, K. *J. Mater. Sci. Lett.* **2001**, *20*, 1483.
15. Konan, K. L.; Peyratout, C.; Smith, A.; Bonnet, J.-P.; Magnoux, P.; Ayrault, P. *J. Colloid Interface Sci.* **2012**, *382*, 17.
16. Jeong, E.; Lim, J. W.; Seo, K. W.; In, S. J.; Lee, Y. S. *J. Ind. Eng. Chem.* **2011**, *17*, 77.
17. Tamura, K.; Yokoyama, S.; Pascua, C. S.; Yamada, H. *Chem. Mater.* **2008**, *20*, 2242.
18. Liu, Y. L.; Wei, W. L.; Hsu, K. Y.; Ho, W. H. *Thermochim. Acta* **2004**, *412*, 139.
19. Rutkai, G.; Makó, É.; Kristóf, T. *J. Colloid Interface Sci.* **2009**, *334*, 65.
20. Credoz, A.; Bildstein, O.; Jullien, M.; Raynal, J.; Trotignon, L.; Pokrovsky, O. *Appl. Clay Sci.* **2011**, *53*, 402.
21. Wattanasiriwech, D.; Wattanasiriwech, S. *J. Eur. Ceram. Soc.* **2011**, *31*,1371.
22. Wattansiriwech, D.; Srijan, K.; Wattanasiriwech, S. *Appl. Clay Sci.* **2009**, *43*, 57.
23. Cornell, R. M. *J. Radioanal. Nucl. Chem.* **1993**, *171*, 483.
24. Benedicto, A.; Missana, T.; Fernández, A. M. *Environ. Sci. Technol.* **2014**, *48*, 4909.
25. Christidis, G. E.; Scott, P. W.; Dunham, A. C. *Appl. Clay Sci.* **1997**, *12*, 329.
26. Woumfo, D.; Kamga, R.; Figueras, F.; Njopwouo, D. *Appl. Clay Sci.* **2007**, *37*, 149.
27. Korichi, S.; Elias, A.; Mefti, A. *Appl. Clay Sci.* **2009**, *42*, 432.
28. Yuan, P.; Tan, D. Y.; Annabi-Bergaya, F.; Yan, W. C.; Liu, D.; Liu, Z. W. *Appl. Clay Sci.* **2013**, *83–84*, 68.
29. Heller-Kallai, L. *Clay Miner.* **1991**, *26*, 245.
30. Valášková, M.; Rieder, M.; Matějka, V.; Čapková, P.; Slíva, A. *Appl. Clay Sci.* **2007**, *35*, 108.
31. Xue, B.; Zhang, P. P.; Jiang, Y. S.; Sun, M. M.; Liu, D. R.; Yu, L. X. J. *Appl. Polym. Sci.* **2011**, *120*, 1736.
32. Xue, B.; Jiang, Y. S.; Li, G. D. *Polym. Compos.* **2013**, *34*, 1061.
33. Madejová, J.; Pentrák, M.; Pálková, H.; Komadel, P. *Vib. Spectrosc.* **2009**, *49*, 211.
34. Mbey, J. A.; Thomas, F.; Ngally Sabouang, C. J.; Liboum, D.; Njopwouo, D. *Appl. Clay Sci.* **2013**, *83–84*, 327.
35. Mosser-Ruck, R. *Clay Miner.* **2003**, *38*, 201.
36. Risberg, E. D.; Mink, J.; Abbasi, A.; Skripkin, M. Y.; Hajba, L.; Lindqvist-Reis, P.; Bencze, E.; Sandström, M. *Dalton T.* **2009**, *8*, 1328.
37. Ratna, D.; Divekar, S.; Samui, A. B.; Chakraborty, B. C.; Banthia, A. K. *Polymer* **2006**, *47*, 4068.
38. Reddy, M. J.; Chu, P. P.; Rao, U. V. S. *J. Power Sources* **2006**, *158*, 614.
39. Burgaz, E.; Yazici, M.; Kapusuz, M.; Alisir, S. H.; Ozcan, H. *Thermochim. Acta* **2014**, *575*, 159.
40. Aranda, P.; Ruiz-Hitzky, E. *Chem. Mater.* **1992**, *4*, 1395.
41. Papke, B. L.; Ratner, M. A.; Shriver, D. F. *J. Phys. Chem. Solids* **1981**, *42*, 493.
42. Aranguren, M. I.; Mora, E.; DeGroot, J. V.; Macosko, C. W. *J. Rheol.* **1992**, *36*, 1165.
43. Wunderlich, B. Macromolecular Physics; Academic: New York, **1980**.
44. Chen, H.-W.; Chang, F.-C. *Polymer* **2011**, *42*, 9763.
45. McNeill, I. C.; Zulfiqar, M.; Kousar, T. *Polym. Degrad. Stab.* **1990**, *28*, 131.